Journal of Materials Chemistry A

ROYAL SOCIETY OF CHEMISTRY

PAPER

View Article Online
View Journal | View Issue



Cite this: J. Mater. Chem. A, 2024, 12, 19950

# Designing atomic Ni/Cu pairs on a reactive BiOCl surface for efficient photo-chemical $HCO_3^-$-to-CO conversion†

Da Ke,‡[a] Bingjie Sun,‡[a] Yanjun Zhang,‡[b] Fan Tian,[b] Yu Chen,[c] Qingwen Meng,[a] Yixuan Zhang,[a] Zhangyi Hu,[a] Hongzhou Yang,[a] Chenyu Yang,[a] Xuyang Xiong *[a] and Tengfei Zhou *[a]

Received 2nd April 2024
Accepted 3rd June 2024

DOI: 10.1039/d4ta02199a

rsc.li/materials-a



Solar-driven conversion of bicarbonate ($HCO_3^-$) to carbonaceous fuels and/or chemicals provides an alternative route for the development of sustainable carbon economies. However, promoting the $HCO_3^-$ reduction rate and tuning product selectivity remain significant challenges. This study reports the identification of isolated Ni/Cu atomic pairs dispersed on a BiOCl surface ($Ni_1/Cu_1$-BOC) as a promising candidate for efficient $HCO_3^-$ reduction under UV-vis light irradiation. The optimized photocatalyst exhibits a high CO formation rate of 157.1 μmol $g^{-1}$ $h^{-1}$ with nearly 100% selectivity, even in the absence of added proton sources, sacrificial agents, or sensitizers. Experimental and theoretical investigations reveal that the atomically dispersed Ni/Cu pairs facilitate the protonation of $HCO_3^-$ to $CO_2$, which then undergoes a $H^+$-assisted reduction pathway to produce CO, with *COOH as the intermediate. The synergistic effects of the Ni/Cu atomic pairs simultaneously promote the $HCO_3^-$-to-$CO_2$ conversion and the subsequent $CO_2$-to-CO reduction, providing valuable insights for the development of efficient diatomic catalysts for photocatalytic $HCO_3^-$ reduction reactions.

## Introduction

Direct photocatalytic reduction of bicarbonate ($HCO_3^-R$) using naturally abundant carbonate/bicarbonate minerals as the feedstock, without additional $CO_2$ supplementation in aqueous media, is a challenging yet fascinating approach for the development of economical carbon-resource conversion technologies.[1] The dissolved $HCO_3^-$ inevitably undergoes dissociation ($HCO_3^- \rightarrow CO_2$ (aq) + $OH^-$) and/or protonation ($HCO_3^- + H^+ \rightarrow CO_2$ (aq) + $H_2O$) processes, resulting in a near-zero concentration of $CO_2$, which then needs to be further reduced to carbonaceous products.[2,3] This $CO_2$-mediated $HCO_3^-$ conversion rate is kinetically sluggish due to the ultra-low $CO_2$ concentration and the unfavourable alkaline pH that restricts $CO_2$ formation.[4] Moreover, the excessive presence of $HCO_3^-$ anions on the $CO_2$ reduction ($CO_2R$) sites prevents the adsorption and activation of $CO_2$ molecules, further lowering the overall activity.[5,6] Therefore, designing catalysts to enhance local $CO_2$(aq) concentration with specific $HCO_3^-/CO_2$ conversion sites is crucial for the high-performance $HCO_3^-R$ reaction.

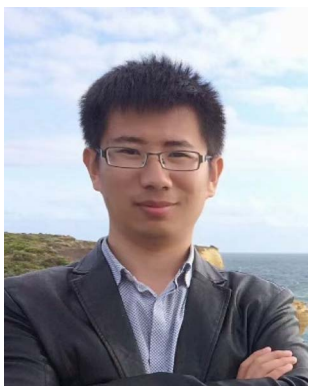

Tengfei Zhou

*Prof. Tengfei Zhou's research is focused on $CO_2$ conversion, metal–$CO_2$ batteries, low-temperature batteries and interfacial catalysis problems encountered in energy storage systems. Zhou started his professional research career as an Australian Research Council (ARC) DECRA Fellow in the Institute for Superconducting and Electronic Materials at the University of Wollongong from 2018 to 2021, under the supervision of Prof. Zaiping Guo. He is currently a professor at the Institutes of Physical Science and Information Technology at Anhui University.*

[a]Institutes of Physical Science and Information Technology, Key Laboratory of Structure and Functional Regulation of Hybrid Material (Ministry of Education), Anhui University, Hefei 230601, China. E-mail: tengfeiz@ahu.edu.cn; xuyang@ahu.edu.cn

[b]School of Chemistry and Environmental Engineering, Wuhan Institute of Technology, Wuhan, 430205, China

[c]Shanghai Synchrotron Radiation Facility, Shanghai Advanced Research Institute, Chinese Academy of Sciences, Shanghai, 201204, China

† Electronic supplementary information (ESI) available. See DOI: https://doi.org/10.1039/d4ta02199a

‡ These authors contributed equally.

Recent studies have shown that $H^+$-driven $HCO_3^-$ speciation through long-range proton transport (~100 nm) can efficiently promote the local $CO_2R$ rate compared to $HCO_3^-$ self-dissociation.[7] The $H^+$ generated from nearby redox sites can directly react with $HCO_3^-$ and/or $OH^-$ to generate *in situ* $CO_2$(aq), which can then undergo $H^+$-assisted $CO_2R$ to carbonaceous products, thereby facilitating the entire $HCO_3^-R$ process.[8,9] However, the use of external proton sources, such as inorganic/organic acids (HCl, $H_2SO_4$, and $H_2BQ$) or organic additives (EtOH and MeOH) and buffer solution ($NaH_2PO_4/Na_2HPO_4$), not only adds extra costs to the $HCO_3^-R$ systems but also introduces undesirable corrosion of the reactors.[10–12] Additionally, the presence of $H^+$ can competitively consume photo-induced electrons, further lowering the reaction activity and selectivity.[13] Therefore, developing cost-effective proton sources (particularly $H_2O$) that can provide $H^+$ under neutral conditions, and novel catalysts that selectively reduce $CO_2$, are crucial priorities for the practical development of efficient $HCO_3^-R$ systems.

Single atomic catalysts (SACs) with highly exposed reactive sites, unsaturated coordinate geometries, and unique chemical/physical properties have garnered extensive research interest in the fields of $CO_2$ reduction, $N_2$ fixation and $H_2O$ splitting.[14–16] The isolated, dispersed metal sites in SACs may outperform metal clusters/alloys in selective chemical conversion to target products, as they are less susceptible to competing reactions due to their single-type atomic geometry, particularly in $H^+$-assisted molecular catalysis that prevents undesirable $H_2$ formation.[17] For instance, manipulating Ni single atoms on carbon nitride/$ZrO_2$ substrates to form Ni-based SACs has favoured electro/photo-chemical $CO_2$ reduction to CO with >99% CO Faraday efficiency and/or ~100% CO selectivity, even in aqueous media.[18,19] However, while known SACs comprising noble metals (Ru, Ir and Re) and earth-abundant metals (Co, Ni and Fe) can reduce $CO_2$ to CO, relatively few of them can realize $HCO_3^-R$.[20–26] The $CO_2$-to-CO undergoes a $2e^-/2H^+$ transfer process, while $HCO_3^-$-to-CO requires an additional $H^+$ to pre-generate $CO_2$(aq). Incorporating metals capable of accomplishing multi-$e^-/H^+$ transfer/formation into SACs as catalytic pairs could theoretically drive the $HCO_3^-$ reduction reaction.[27] Previous work has demonstrated a self-adaptive dual-metal-site catalyst (DMSC) with flexible Ni–Cu pairs that can reduce $CO_2$ to $CH_4$,[28,29] motivating the design of photocatalysts with Ni/Cu catalytic pairs for $HCO_3^-R$ attempts.

Herein, we present a PVP-mediated solvothermal method for fabricating a diatomic catalyst by immobilizing Ni and Cu single atoms on the photoreactive (001) surface of BiOCl (abbreviated as $Ni_1/Cu_1$-BOC). The single-site Ni and Cu atoms in their respective forms enabled photocatalytic $CO_2R$ and $HCO_3^-R$ under mild conditions without the assistance of sacrificial agents or photosensitizers. $Ni_1/Cu_1$-BOC exhibited an impressive $HCO_3^-$-to-CO (in aqueous media) reduction rate of around 157.1 μmol $g^{-1}$ $h^{-1}$, with nearly 100% CO selectivity, outperforming the individual $Ni_1$-BOC (115.2 μmol $g^{-1}$ $h^{-1}$), $Cu_1$-BOC (89.1 μmol $g^{-1}$ $h^{-1}$) and pristine BOC (34.6 μmol $g^{-1}$ $h^{-1}$) catalysts. Detailed characterization revealed that the CO formation was closely correlated with the local $CO_2$(aq) from the protonation of $HCO_3^-R$, resulting in a $CO_2$-intermediated $HCO_3^-R$ mechanism. *In situ* Fourier-transform infrared spectroscopy (*in situ* FTIR) and density functional theory (DFT) calculations confirmed that the Ni/Cu catalytic pairs controlled the reaction path to CO by significantly promoting *COOH as the intermediate and reducing the energy barriers for CO formation.

## Results and discussion

The synthetic procedure for the $Ni_1/Cu_1$-BOC photocatalyst is described in Fig. 1a. $NiCl_2 \cdot 6H_2O$, $CuCl_2 \cdot 2H_2O$ and $Bi(NO_3)_3 \cdot 5H_2O$ respectively served as $Ni^{2+}$, $Cu^{2+}$ and $Bi^{3+}/Cl^-$ sources with ethylene glycol (EG) as the solvent. During the solvothermal stage, PVP (K30) was added as a surface-mediating agent to create more sites for the immobilization of singly dispersed Cu and Ni on the BiOCl substrate. PVP can also prevent the agglomeration of BiOCl nanoparticles, favoring the crystallization of BiOCl in well-defined morphologies with large specific surface areas.[30] Other control photocatalysts, namely $Ni_1$-BOC, $Cu_1$-BOC and BOC, were prepared using a similar synthetic method. The Ni and Cu loadings in the different photocatalysts were quantified by inductively coupled plasma optical emission spectroscopy (ICP-OES) (Table S1†).

The XRD patterns of the $Ni_1/Cu_1$-BOC, $Ni_1$-BOC and $Cu_1$-BOC photocatalysts showed only the typical reflection peaks of tetragonal BiOCl, indicating that any Ni and Cu were highly dispersed on the support (Fig. 1b). Raman spectra of these photocatalysts also showed identical vibration peaks $A_{1g}{}^2$ internal Bi–Cl phonon mode (145 $cm^{-1}$) and $E_g$ internal Bi–Cl phonon mode (190 $cm^{-1}$) to that of BiOCl,[31] suggesting that the Ni and Cu were not incorporated by interlaminar Cl atoms (Fig. 1c). TEM images revealed that the $Ni_1/Cu_1$-BOC photocatalyst had a square-like morphology and was free of any irregular impurities or clusters (Fig. 1d). High-resolution TEM (HRTEM) images for the selected regions showed sets of interlaced lattice fringes, with interplanar spacings of around 0.27 nm which were well-crystallized along the [001] direction (Fig. 1e and S1†). Energy dispersive spectroscopy (EDS) elemental mapping images for Bi, O, Cl, Ni and Cu revealed a uniform distribution of these elements in the entire $Ni_1/Cu_1$-BOC nanosheets (Fig. 1f).

To probe the coordination structures of Ni and Cu atoms in the $Ni_1/Cu_1$-BOC photocatalyst, Ni and Cu K-edge X-ray absorption near-edge structure (XANES), extended X-ray absorption fine structure (EXAFS) and wavelet transform (WT) data were collected for $Ni_1/Cu_1$-BOC and related reference materials. As shown in Fig. 2a, the Ni K-edge of $Ni_1/Cu_1$-BOC and $Ni_1$-BOC exhibited higher pre-edge energies than that of Ni foil and NiO, indicating that the Ni center in $Ni_1/Cu_1$-BOC and $Ni_1$-BOC had a higher valence state than NiO. The Ni K-edge EXAFS spectra of $Ni_1/Cu_1$-BOC and $Ni_1$-BOC showed one intense peak at approximately 1.3 Å, closely related to the first shell of Ni–O coordination possibly due to the embedded Ni in the $[Bi_2–O_2]^{2+}$ matrix (Fig. 2b). No Ni–Ni bond (2.17 Å for Ni foil and 2.34 Å for NiO) was observable in $Ni_1/Cu_1$-BOC and $Ni_1$-BOC, indicating that Ni atoms were singly dispersed. The atomic dispersion of Ni species in $Ni_1/Cu_1$-BOC and $Ni_1$-BOC

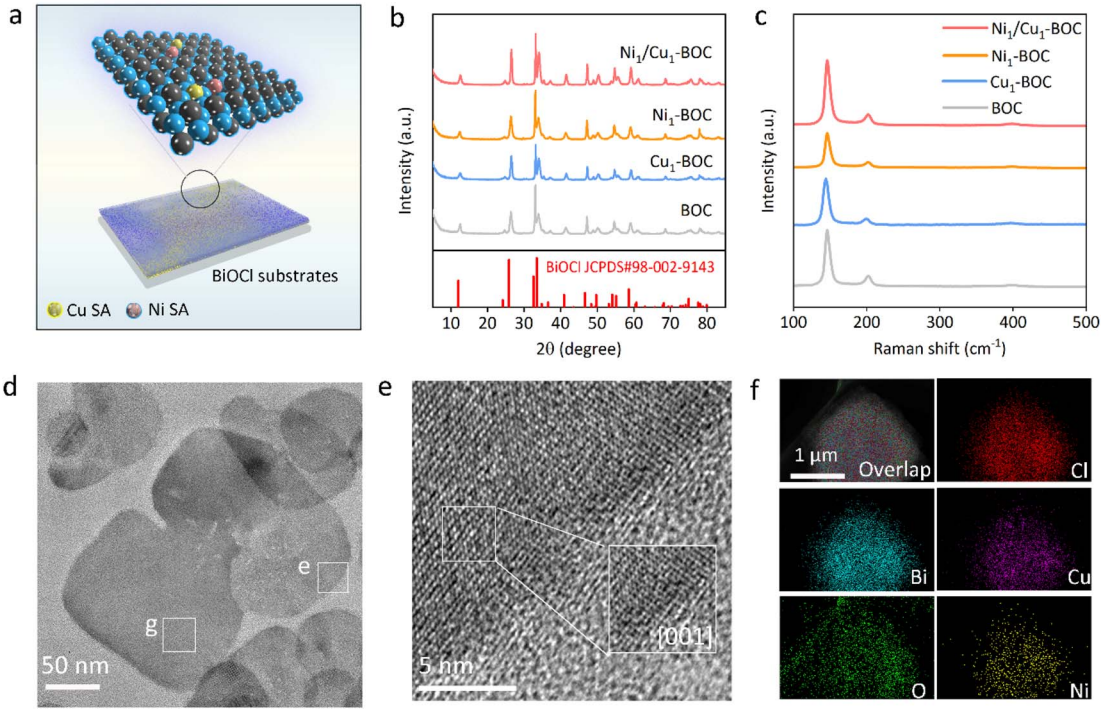


Fig. 1 (a) Scheme depicting the synthesis of $Ni_1/Cu_1$-BOC. (b and c) XRD patterns and Raman spectra of $Ni_1/Cu_1$-BOC, $Ni_1$-BOC, $Cu_1$-BOC and BOC. (d–f) TEM, HRTEM and EDS mapping images of $Ni_1/Cu_1$-BOC.

was further confirmed by WT analysis of Ni K-edge EXAFS oscillations. The WT contour plots of $Ni_1/Cu_1$-BOC and $Ni_1$-BOC showed maximum intensities attributable to Ni–O bonding (at 4.9 and 4.8 $Å^{-1}$, respectively), whereas the Ni–Ni bonding was absent (Fig. 2c).[32] Fig. 2d shows the Cu K-edge XANES spectra of $Ni_1/Cu_1$-BOC, $Cu_1$-BOC, Cu foil and CuO. The Cu K-edge of $Ni_1/Cu_1$-BOC and $Cu_1$-BOC was close to that of CuO, suggesting that Cu atoms in $Ni_1/Cu_1$-BOC and $Cu_1$-BOC were positively charged with valence states near +2. The Cu K-edge EXAFS spectra of $Ni_1/Cu_1$-BOC and $Cu_1$-BOC showed peaks only assigned to the Cu–O bond (1.5 Å) while Cu–Cu interactions (2.24 Å for Cu foil and 2.46 Å for CuO) were undetectable (Fig. 2e). This indicated that Cu atoms in $Ni_1/Cu_1$-BOC and $Cu_1$-BOC were also isolated and dispersed, for which the WT contour plots of $Ni_1/Cu_1$-BOC demonstrated different Cu features than that of Cu foil and CuO (Fig. 2f). To better understand the electronic and spatial structures of Ni and Cu atoms in the $Ni_1/Cu_1$-BOC photocatalyst, Ar ion sputtering and high-resolution X-ray photoelectron spectroscopy (XPS) were performed over the Ni 2p, Cu 2p, Bi 4f, O 1s, and Cl 2p regions of $Ni_1/Cu_1$-BOC along with selected reference samples including $Ni_1$-BOC, $Cu_1$-BOC and BOC. As shown in Fig. 2g, the Ni 2p spectra of $Ni_1/Cu_1$-BOC was deconvoluted into five peaks including $Ni^{2+}$ ($2p_{3/2}$ 855.4 eV and $2p_{1/2}$ 873 eV), $Ni^{\delta+,\delta>2}$ ($2p_{3/2}$ 857.3 eV) and $Ni^{2+}$ shake up satellites (880.2 eV and 861.4 eV).[33] This evidenced the presence of over-oxidized Ni, consistent with the afore-analyzed Ni K-edge XANES results. The Ni 2p signals almost vanished after Ar ion sputtering, implying that Ni single atoms were mainly dispersed on the outermost surfaces of $Ni_1/Cu_1$-BOC. Fig. 2h shows the Cu 2p spectra of $Ni_1/Cu_1$-BOC. The intense peak centered at 940.5 eV was ascribed to Bi 4s orbitals while peaks at 932.1 eV and 951.0 eV were assigned to $Cu^{2+}$ cations.[34] The Cu atoms were also localized on the outermost layer of $Ni_1/Cu_1$-BOC, and its oxidative states were rarely influenced by Ni loading (Fig. S2†). The Bi 4f spectra of $Ni_1/Cu_1$-BOC are depicted in Fig. 2i. Two peaks at 158.4 eV and 164.4 eV were clearly resolved, related to partially reduced $Bi^{3-x}$ states. The surface Bi atoms were relatively negatively charged in contrast to the inner form, indicating that Bi atoms were unconventionally coordinated. This might be attributed to the additives Ni and Cu in the BiOCl substrate, which significantly modified the delocalized electrons near Bi, O and Cl atoms, thus altering the redox capacity (Fig. S3†).

The photocatalytic $HCO_3^-$R experiments were performed under UV-vis light irradiation without any assistance of photosensitizers and sacrificial agents. Prior to each test, the custom-built photoreactor was purged using high-purity Ar to eliminate gaseous impurities. Fig. 3a shows that $Ni_1$-BOC delivered a $HCO_3^-$-to-CO production rate of 115.2 μmol $g^{-1}$ $h^{-1}$, much higher than that of BOC (34.6 μmol $g^{-1}$ $h^{-1}$). After the introduction of Cu single atoms, the photocatalytic activity was further improved. $Ni_1/Cu_1$-BOC offered the highest CO formation rate of 157.1 μmol $g^{-1}$ $h^{-1}$, which was 1.4, 1.8 and 4.5 times higher than the activities of $Ni_1$-BOC, $Cu_1$-BOC and the BOC reference photocatalyst, respectively. The $H_2$ formation was negligible during CO production, probably due to the alkaline $HCO_3^-$R conditions that prevent $H^+$-coupling. This superb $HCO_3^-$R rate demonstrated by $Ni_1/Cu_1$-BOC could also be extended to the $CO_2$R reaction, where humid $CO_2$ gas replaced aqueous $HCO_3^-$ solution as the catalytic feed. As shown in Fig. 3b, $Ni_1/Cu_1$-BOC afforded the optimal $CO_2$R performance

 

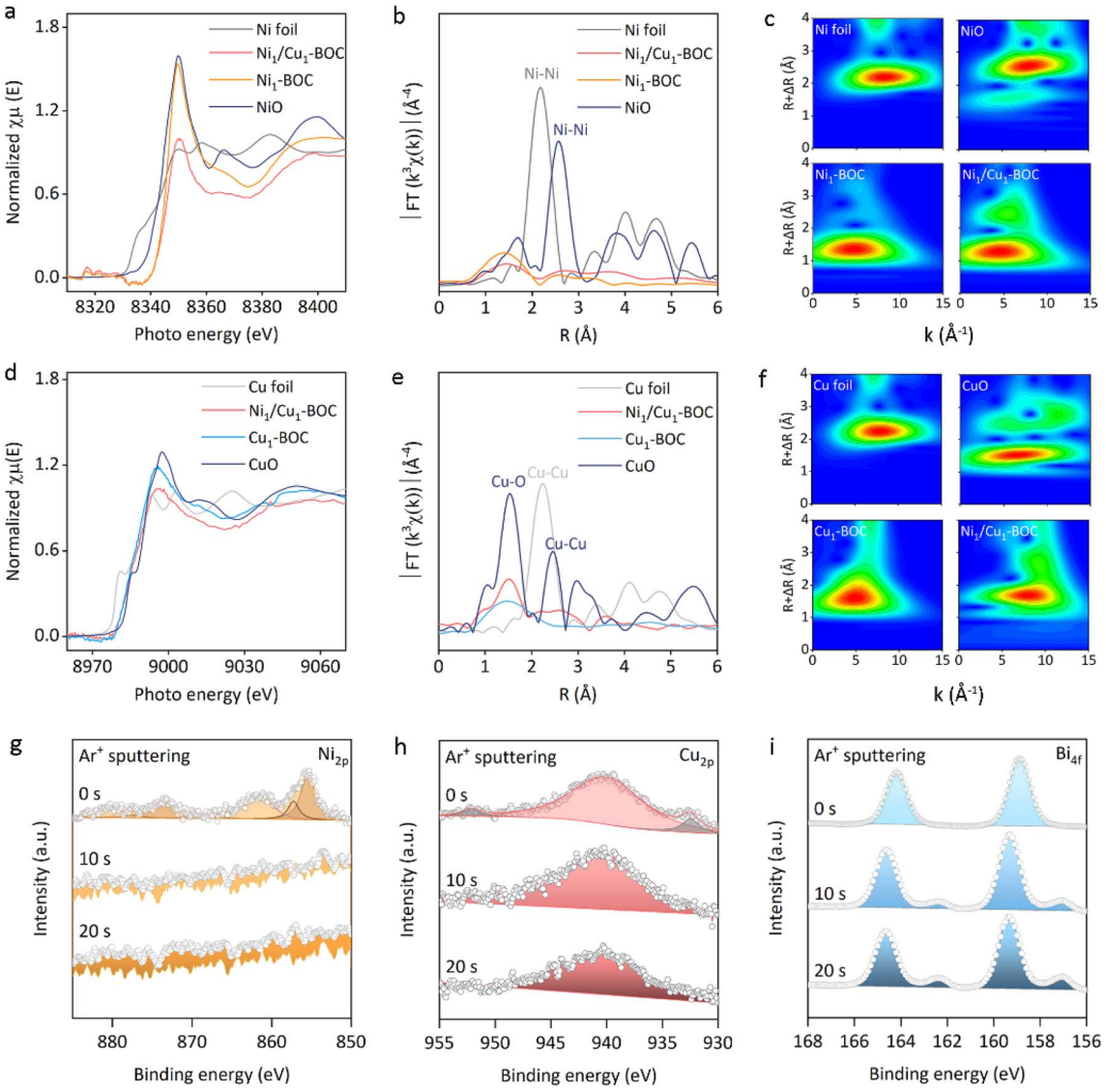


Fig. 2 (a) Ni K-edge XANES spectra, (b) $k^3$-weighted Fourier transforms of the Ni K-edge EXAFS spectra and (c) relative WT plots of Ni foil, $Ni_1/Cu_1$-BOC, $Ni_1$-BOC and a NiO standard. (d) Cu K-edge XANES spectra, (e) $k^3$-weighted Fourier transforms of the Cu K-edge EXAFS spectra and (f) relative WT plots of Cu foil, $Ni_1/Cu_1$-BOC, $Cu_1$-BOC and a CuO standard. (g–i) Ar ion sputtering X-ray photoelectron spectra of Ni 2p, Cu 2p and Bi 4f orbitals in $Ni_1/Cu_1$-BOC.

amongst $Ni_1$-BOC, $Cu_1$-BOC and BOC catalysts. The CO produced from $CO_2$ was less than that from $HCO_3^-$, which might be because of the lower solubility of $CO_2$ in aqueous media. Fig. 3c shows the $HCO_3^-$R results over $Ni_1/Cu_1$-BOC at different pH values. The CO formation rate was dramatically increased by $H^+$ addition, and suppressed under excessively alkaline conditions. Based on the Bjerrum plot, the fraction of water-soluble $CO_2$ was nearly 0 at pH > 8.5.[7] This could be utilized to explain the almost 0 μmol $g^{-1}$ $h^{-1}$ CO formation rate at pH ≈ 9, because $HCO_3^-$ might not evolve into $CO_2$ thus suspending the overall $HCO_3^-$-to-CO conversion. Lowering the pH value to a neutral value and/or increasing the local $CO_2$ contents could promote CO production, further evidencing that $CO_2$ was the key intermediate during the $HCO_3^-$R reaction. Cycling experiments of $Ni_1/Cu_1$-BOC showed no decrease in the CO formation after 5 runs, indicating that the photocatalyst possessed good photostability (Fig. S4†). XRD patterns and TEM images of $Ni_1/Cu_1$-BOC before and after the reaction were almost identical, suggesting that Ni/Cu catalytic pairs were stable against aggregating during the photocatalytic tests (Fig. S5†). To gain deeper insights into the mechanism underpinning the fast $HCO_3^-$R conversion on $Ni_1/Cu_1$-BOC as compared with BOC, *in situ* FTIR spectra were deliberately employed to monitor the reaction details. As shown in Fig. 3d and e, IR spectra of $Ni_1/Cu_1$-BOC and BOC showed peak positions ranging from 1200 to 1700 $cm^{-1}$, respectively assigned to chemisorption $CO_2$ ($^*CO_2^-$, 1248 $cm^{-1}$, 1700 $cm^{-1}$), bicarbonates ($HCO_3^-$, 1400–1435 $cm^{-1}$), monodentate carbonates (m-$CO_3^{2-}$, 1381 $cm^{-1}$ and 1451 $cm^{-1}$) and bidentate carbonates (b-$CO_3^{2-}$, 1357 $cm^{-1}$ and 1556 $cm^{-1}$).[35–37] The intensity of these peaks intensified on

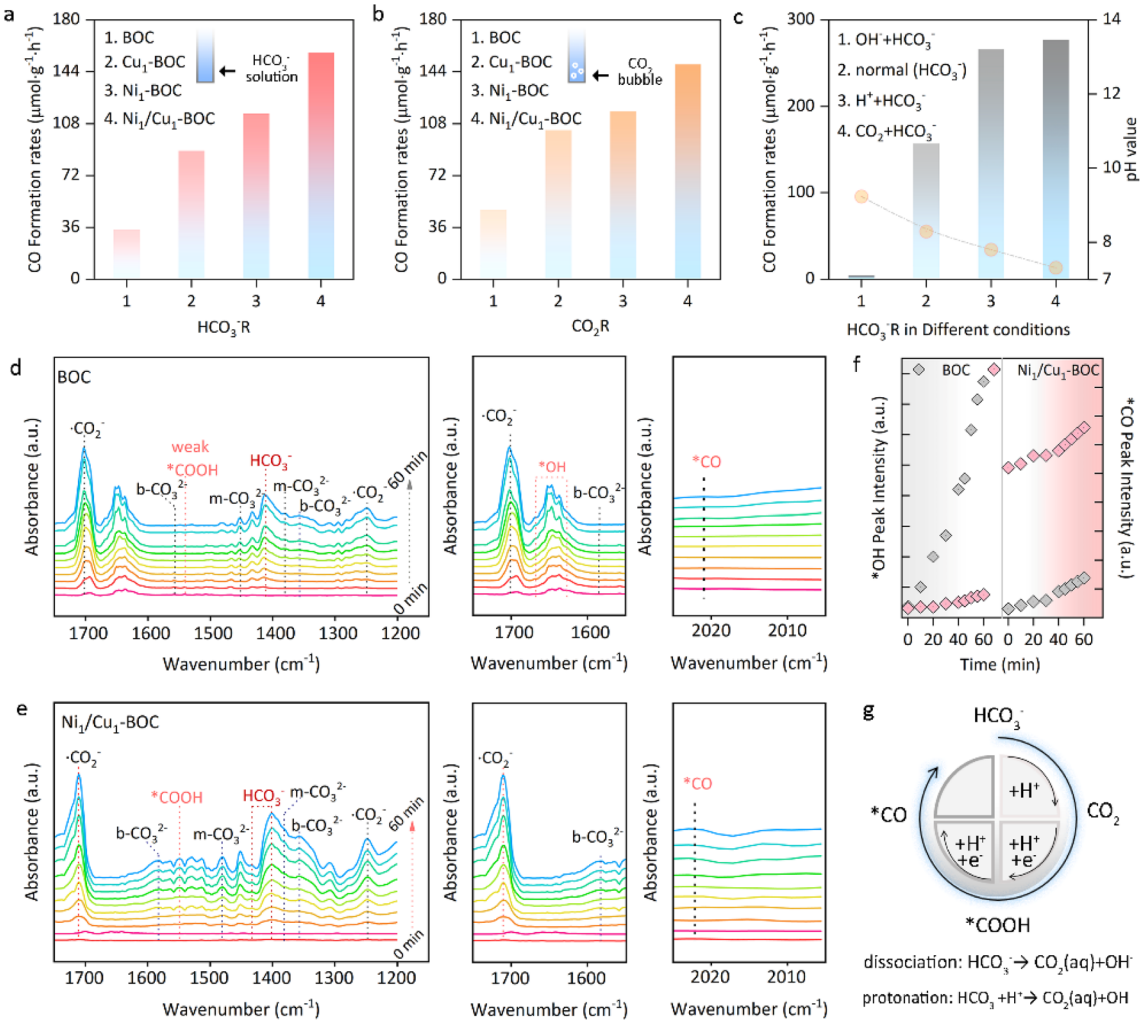


Fig. 3 (a) CO production rates from $HCO_3^-$R collected over $Ni_1/Cu_1$-BOC, $Ni_1$-BOC, $Cu_1$-BOC and BOC. Reaction conditions: 1 mol per L $HCO_3^-$ aqueous solution, full spectrum irradiation and 10 mg of the catalyst. (b) CO production rates from $CO_2$R collected over $Ni_1/Cu_1$-BOC, $Ni_1$-BOC, $Cu_1$-BOC and BOC. (c) CO formation rates of $Ni_1/Cu_1$-BOC under different pH conditions. (d and e) *In situ* FTIR spectra of BOC and $Ni_1/Cu_1$-BOC during photocatalytic $HCO_3^-$R reactions. (f) *OH and *CO signals of BOC and $Ni_1/Cu_1$-BOC collected from the *in situ* FTIR spectra. (g) Schematic diagrams showing the $HCO_3^-$R mechanism over $Ni_1/Cu_1$-BOC.

prolonging the irradiation time, indicating that carbonaceous species accumulated on the catalyst surfaces. The obvious differences between $Ni_1/Cu_1$-BOC and BOC were the symmetric IR peaks centered at 1650 and 1540 $cm^{-1}$, which can be readily indexed as the *OH (–OH in $H_2O$) and *COOH groups.[38,39] The *OH signal gradually increased on BOC and almost vanished on $Ni_1/Cu_1$-BOC, implying that $Ni_1/Cu_1$-BOC was unfavourable for *OH or $H_2O$ adsorption in contrast to BOC. The *COOH peak of $Ni_1/Cu_1$-BOC was strengthened compared to that of BOC, evidencing that $Ni_1/Cu_1$-BOC facilitated protonation during the $HCO_3^-$R process with *COOH as the intermediate. Fig. 3f directly provides IR peak intensities of *OH and *CO collected over $Ni_1/Cu_1$-BOC and BOC. The *CO formation slope showed negative correlation with the surface *OH uptake, clearly emphasizing that excess *OH impeded $HCO_3^-$-to-CO conversion. This phenomenon can be explained as *OH consumed additional $H^+$ involved in $HCO_3^-$-to-$CO_2$ and $CO_2$-to-CO paths, thus weakening $CO_2$/*COOH evolution as well as lowering the CO production. The afore-mentioned analysis depicted a typical $HCO_3^-$R route through $HCO_3^-$-$CO_2$-*COOH–CO, during which $Ni_1/Cu_1$-BOC outperformed BOC in CO formation due to its efficiency in $H^+$ utilization (Fig. 3g).

Note that the multi-protons/electron transfer process was involved in $HCO_3^-$-to-CO conversion, and the photoelectric properties and electron-migration capacities of $Ni_1/Cu_1$-BOC and BOC were then respectively investigated. Fig. 4a displays the light absorption characteristics of $Ni_1/Cu_1$-BOC and BOC. The BOC sample had an adsorption edge near 380 nm, arising from the O 2p to Bi 6p transitions. $Ni_1/Cu_1$-BOC showed additional peaks ranging from 400–700 nm, involving O 2p to Ni/Cu 3d transitions and d–d transitions in Ni/Cu 3d orbitals, respectively. The band gap values of $Ni_1/Cu_1$-BOC and BOC were calculated to be 3.31 eV and 3.46 eV based on the Kubelka–Munk function, clearly emphasizing that Ni/Cu incorporation

 

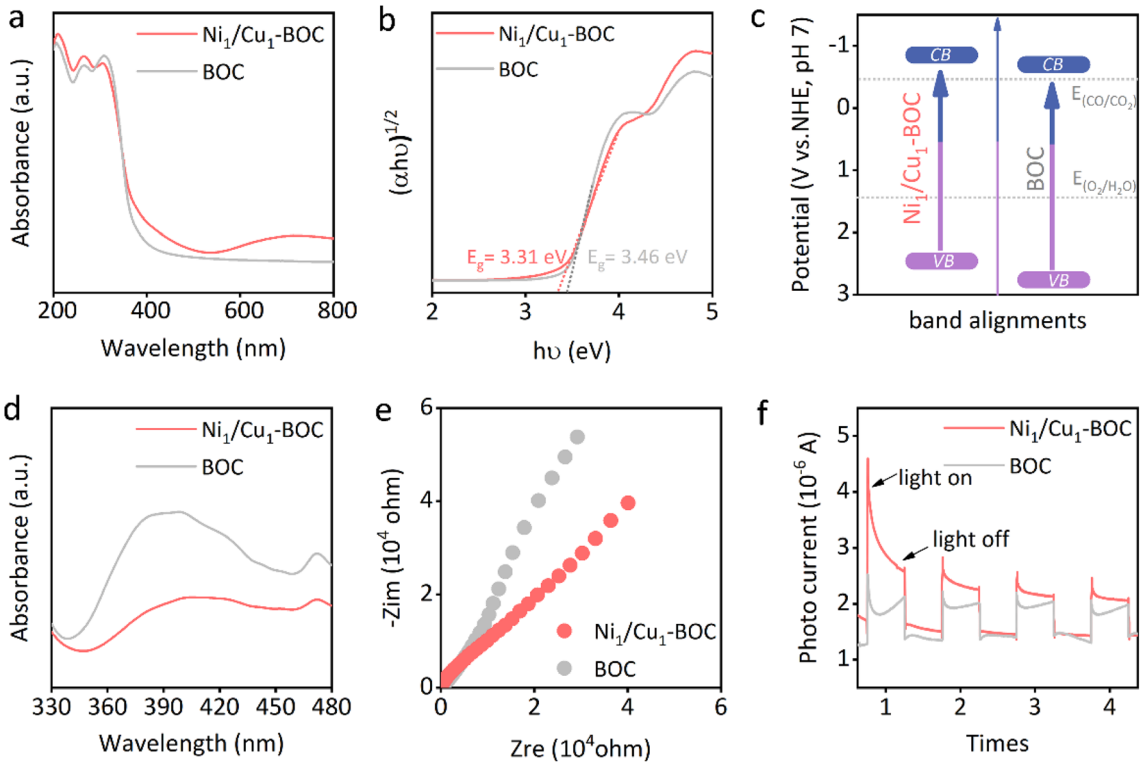


Fig. 4 (a and b) Diffuse reflectance spectra and Tauc plots of $Ni_1/Cu_1$-BOC and BOC. (c) Band alignments of $Ni_1/Cu_1$-BOC and BOC. (d–f) Steady-state PL spectra, EIS and photocurrent patterns of $Ni_1/Cu_1$-BOC and BOC.

changed the intrinsic band alignment of BiOCl (Fig. 4b). The conduction band (CB) levels of $Ni_1/Cu_1$-BOC and BOC were determined to be −0.85 V and −0.7 V (*vs.* NHE) from the Mott–Schottky plots, all satisfying the thermodynamic requirements for CO production from $CO_2$ (Fig. S6†).[40] Additionally, the valence band (VB) positions of $Ni_1/Cu_1$-BOC and BOC were estimated to be about 2.46 eV and 2.76 eV, all above the redox potential for $H_2O$ oxidation to $O_2$ (Fig. 4c).[41] This observation suggested that CO and $O_2$ possibly served as the products from reduction/oxidation-half reactions, with pre-analyzed surface *OH probably being the oxygen evolution intermediate.[42] The dynamics of photo-induced charge carriers were then employed by photoluminescence (PL) and electrochemical impedance spectroscopy (EIS). As shown in Fig. 4d and e, $Ni_1/Cu_1$-BOC displayed weakened PL peaks with the smallest EIS semicircles as compared with BOC. Note that the quenched PL signals reflected the suppressed electron–hole recombination and the EIS radius empirically correlated with the inner-resistance; the afore-mentioned results thus collectively indicated that $Ni_1/Cu_1$-BOC possessed the best charge separation efficiency due to its high conductivity.[43–48] Fig. 4f shows the photocurrent signals collected over $Ni_1/Cu_1$-BOC and BOC during the same time interval. The photovoltaic peaks demonstrated by $Ni_1/Cu_1$-BOC surpassed that of BOC, further evidencing that $Ni_1/Cu_1$-BOC facilitated photoelectric conversion and charge carrier migration.[49–51]

To further elucidate the photocatalytic $HCO_3^-$R dynamics at the atomic level, DFT calculations of elementary $HCO_3^-$R steps over $Ni_1/Cu_1$-BOC and BOC were separately simulated. Based on the XAFS studies, we constructed surface models as BOC (001) with/without Ni/Cu catalytic pairs (Ni/Cu-BOC and BOC) to represent the likely coordination geometries of $Ni_1/Cu_1$-BOC and BOC samples (Fig. 5a). Fig. 5b shows Gibbs energy barriers

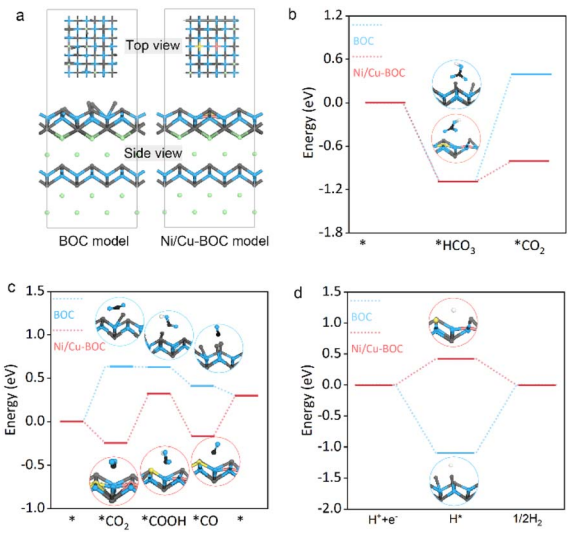


Fig. 5 (a) DFT models representing BOC and $Ni_1/Cu_1$-BOC samples. (b–d) Energy profiles for the elementary steps of $HCO_3^-$-to-$CO_2$, $CO_2$-to-CO and $H^+$-to-$H_2$ pathways over BOC and the Ni/Cu-BOC model.

involved in $HCO_3^-$-to-$CO_2$ conversion. The solvated $HCO_3^-$ anions were first chemically adsorbed on the catalytic surfaces, followed by C–OH cleavage (by dehydration) to form $*CO_2$. Ni/Cu-BOC offered a lower energy barrier for $*HCO_3$ protonation/dehydration to $*CO_2$, evidencing that the $Ni_1/Cu_1$-BOC catalyst favoured $H^+$ utilization. The subsequent transformation of $CO_2$ into CO was predicted to occur endothermically over the Ni/Cu-BOC model, and the formation of adsorbed *COOH was the rate limiting step (Fig. 5c). The summed-up energy barriers required for CO production within the Ni/Cu-BOC model ($\Delta G = 0.57$ eV) also lower than that of the BOC model ($\Delta G = 0.63$ eV), indicating the advantages of Ni/Cu catalytic pairs in $HCO_3^-R/CO_2R$ reactions. The dissociative $H^+$ tended to be captured by BOC as adsorbed *H, while Ni/Cu-BOC unfavoured *H formation thus preferred $H^+$-driven $HCO_3^-$ speciation/$H^+$-assisted $CO_2$ reduction (Fig. 5d).

## Conclusions

In conclusion, a $Ni_1/Cu_1$-BOC photocatalyst comprising singly dispersed Ni/Cu catalytic pairs over a BiOCl substrate afforded excellent performance for the photocatalytic reduction of bicarbonate ($HCO_3^-$) to carbon monoxide (CO) under UV-vis irradiation. Benefiting from the surface-immobilized Ni/Cu catalytic pairs, a remarkable CO formation rate of 157.1 μmol $g^{-1}$ $h^{-1}$ was realized in the $HCO_3^-$ aqueous solution, surpassing the activities of the individual $Ni_1$-BOC, $Cu_1$-BOC and BOC catalysts. *In situ* FTIR results and photoelectric tests showed that the protons and electrons required for the $HCO_3^-$-to-$CO_2$ conversion were dramatically increased and promoted on the Ni/Cu-involved catalyst, facilitating the subsequent $CO_2$ reduction to CO with *COOH as the reactive intermediate. DFT calculations also demonstrated that the Ni/Cu-BOC model lowers the energy barriers involved in the $HCO_3^-$ reduction process by significantly promoting the utilization of $H^+$ through a series of protonation and dehydration pathways leading to CO production. These findings shed light on the rational design of diatomic photocatalysts for sustainable $HCO_3^-/CO_2$ reduction reactions. The $Ni_1/Cu_1$-BOC photocatalyst developed in this study delivers an unusually high CO formation rate during the photocatalytic $HCO_3^-$ reduction tests, showcasing its potential for practical applications in the development of economical carbon-resource conversion technologies.

## Data availability

All the data supporting this article have been included in the main text and the ESI.†

## Author contributions

D. Ke, B. Sun and Y. Zhang: investigation, visualization and writing – original draft. F. Tian and H. Yang: supervision and conceptualization. Y. Chen: resources and software. Q. Meng, Y. Zhang, Z. Hu and C. Yang: data curation, formal analysis and visualization. X. Xiong and T. Zhou: supervision, writing – review & editing, resources and funding acquisition.

## Conflicts of interest

There are no conflicts to declare.

## Acknowledgements

The authors are grateful for the financial support of the Anhui Provincial Natural Science Foundation for Outstanding Young Scholar (2208085Y05), Anhui Provincial Scientific Reuter Foundation for Returned Scholars (2022LCX030), and the National Natural Science Foundation of China (52202198 and 22272207). The authors also thank Dr Yu Chen from the Shanghai Synchrotron Radiation Facility for his help with the XAS data analysis.

## Notes and references

1 C. Hepburn, E. Adlen, J. Beddington, E. Carter, S. Fuss, N. Mac Dowell, J. Minx, P. Smith and C. Williams, *Nature*, 2019, **575**, 87–97.
2 S. Zhang, C. Chen, K. Li, H. Yu and F. Li, *J. Mater. Chem. A*, 2021, **9**, 18785–18792.
3 D. Pimlott, A. Jewlal, Y. Kim and C. Berlinguette, *J. Am. Chem. Soc.*, 2023, **145**, 25933–25937.
4 M. Dunwell, Q. Lu, J. Heyes, J. Rosen, J. Chen, Y. Yan, F. Jiao and B. Xu, *J. Am. Chem. Soc.*, 2017, **139**, 3774–3783.
5 C. Stalder, S. Chao and M. Wrighton, *J. Am. Chem. Soc.*, 1984, **106**, 3673–3675.
6 N. Queyriaux, *ACS Catal.*, 2021, **11**, 4024–4035.
7 R. Yanagi, T. Zhao, M. Cheng, B. Liu, H. Su, C. He, J. Heinlein, S. Mukhopadhyay, H. Tan and D. Solanki, *J. Am. Chem. Soc.*, 2023, **145**, 15381–15392.
8 J. Schneider, H. Jia, J. Muckerman and E. Fujita, *Chem. Soc. Rev.*, 2012, **41**, 2036–2051.
9 Q. Dong, X. Zhang, D. He, C. Lang and D. Wang, *ACS Cent. Sci.*, 2019, **5**, 1461–1467.
10 M. Nielsen, E. Alberico, W. Baumann, H. Drexler, H. Junge, S. Gladiali and M. Beller, *Nature*, 2013, **495**, 85–89.
11 M. Symes and L. Cronin, *Nat. Chem.*, 2013, **5**, 403–409.
12 K. Joya, Y. Joya and H. De Groot, *Adv. Energy Mater.*, 2014, **4**, 1301929.
13 N. Elgrishi, M. Chambers and M. Fontecave, *Chem. Sci.*, 2015, **6**, 2522–2531.
14 A. Wang, J. Li and T. Zhang, *Nat. Rev. Chem*, 2018, **2**, 65–81.
15 S. Ding, M. Hülsey, J. Pérez-Ramírez and N. Yan, *Joule*, 2019, **3**, 2897–2929.
16 Q. Wu and C. Wu, *J. Mater. Chem. A*, 2023, **11**, 4876–4906.
17 X. Yang, A. Wang, B. Qiao, J. Li, J. Liu and T. Zhang, *Acc. Chem. Res.*, 2013, **46**, 1740–1748.
18 H. Yang, S. Hung, S. Liu, K. Yuan, S. Miao, L. Zhang, X. Huang, H. Wang, W. Cai and R. Chen, *Nat. Energy*, 2018, **3**, 140–147.
19 X. Xiong, C. Mao, Z. Yang, Q. Zhang, G. Waterhouse, L. Gu and T. Zhang, *Adv. Energy Mater.*, 2020, **10**, 2002928.
20 S. Takizawa, T. Okuyama, S. Yamazaki, K. Sato, H. Masai, T. Iwai, S. Murata and J. Terao, *J. Am. Chem. Soc.*, 2023, **145**, 15049–15053.

 

21 S. Sato, T. Morikawa, T. Kajino and O. Ishitani, *Angew. Chem., Int. Ed.*, 2013, **52**, 988–992.
22 B. Su, Y. Kong, S. Wang, S. Zuo, W. Lin, Y. Fang, Y. Hou, G. Zhang, H. Zhang and X. Wang, *J. Am. Chem. Soc.*, 2023, **145**, 27415–27423.
23 L. Chen, Z. Guo, X. Wei, C. Gallenkamp, J. Bonin, E. Anxolabéhère-Mallart, K. Lau, T. Lau and M. Robert, *J. Am. Chem. Soc.*, 2015, **137**, 10918–10921.
24 H. Rao, L. Schmidt, J. Bonin and M. Robert, *Nature*, 2017, **548**, 74–77.
25 K. Sun, Y. Huang, Q. Wang, W. Zhao, X. Zheng, J. Jiang and H.-L. Jiang, *J. Am. Chem. Soc.*, 2024, **146**, 3241–3249.
26 X. Yu, M. Sun, T. Yan, L. Jia, M. Chu, L. Zhang, W. Huang, B. Huang and Y. Li, *Energy Environ. Sci.*, 2024, **17**, 2260–2268.
27 B. Mondal, A. Rana, P. Sen and A. Dey, *J. Am. Chem. Soc.*, 2015, **137**, 11214–11217.
28 J. Li, H. Huang, W. Xue, K. Sun, X. Song, C. Wu, L. Nie, Y. Li, C. Liu and Y. Pan, *Nat. Catal.*, 2021, **4**, 719–729.
29 Y. Cai, J. Fu, Y. Zhou, Y. Chang, Q. Min, J. Zhu, Y. Lin and W. Zhu, *Nat. Commun.*, 2021, **12**, 586.
30 Y. Lei, G. Wang, S. Song, W. Fan and H. Zhang, *CrystEngComm*, 2009, **11**, 1857–1862.
31 A. Phuruangrat, S. Thongtem and T. Thongtem, *Appl. Phys. A*, 2020, **126**, 245.
32 T. Zhang, X. Han, H. Yang, A. Han, E. Hu, Y. Li, X. Yang, L. Wang, J. Liu and B. Liu, *Angew. Chem., Int. Ed.*, 2020, **59**, 12055–12061.
33 S. Uhlenbrock, C. Scharfschwerdt, M. Neumann, G. Illing and H. Freund, *J. Phys.: Condens. Matter*, 1992, **4**, 7973–7978.
34 S. Poulston, P. Parlett, P. Stone and M. Bowker, *Surf. Interface Anal.*, 1996, **24**, 811–820.
35 Y. Zhang, Z. Xu, Q. Wang, W. Hao, X. Zhai, X. Fei, X. Huang and Y. Bi, *Appl. Catal., B*, 2021, **299**, 120679.
36 E. Köck, M. Kogler, T. Bielz, B. Klötzer and S. Penner, *J. Phys. Chem. C*, 2013, **117**, 17666–17673.
37 S. Collins, M. Baltanás and A. Bonivardi, *J. Phys. Chem. B*, 2006, **110**, 5498–5507.
38 J. Wu, X. Li, W. Shi, P. Ling, Y. Sun, X. Jiao, S. Gao, L. Liang, J. Xu, W. Yan, C. Wang and Y. Xie, *Angew. Chem., Int. Ed.*, 2018, **57**, 8719–8723.
39 X. Li, Y. Sun, J. Xu, Y. Shao, J. Wu, X. Xu, Y. Pan, H. Ju, J. Zhu and Y. Xie, *Nat. Energy*, 2019, **4**, 690–699.
40 S. Nitopi, E. Bertheussen, S. Scott, X. Liu, A. Engstfeld, S. Horch, B. Seger, I. Stephens, K. Chan and C. Hahn, *Chem. Rev.*, 2019, **119**, 7610–7672.
41 M. Yagi and M. Kaneko, *Chem. Rev.*, 2001, **101**, 21–36.
42 X. Shi, S. Back, T. Gill, S. Siahrostami and X. Zheng, *Chem*, 2021, **7**, 38–63.
43 H. Zhang, C. Wang, H. Luo, J. Chen, M. Kuang and J. Yang, *Angew. Chem., Int. Ed.*, 2023, **62**, e202217071.
44 C. Ban, Y. Wang, Y. Feng, Z. Zhu, Y. Duan, J. Ma, X. Zhang, X. Liu, K. Zhou and H. Zou, *Energy Environ. Sci.*, 2024, **17**, 518–530.
45 J. Ma, D. Wu, Y. Feng, C. Ban, L. Xia, L. Ruan, J. Guan, Y. Wang, J. Meng, J. Dai, L. Gan and X. Zhou, *Nano Energy*, 2023, **115**, 108719.
46 J. Chen, F. Zhang, M. Kuang, L. Wang, H. Wang, W. Li and J. Yang, *Proc. Natl. Acad. Sci. U. S. A.*, 2024, **121**, e2318853121.
47 Y. Shi, G. Zhan, H. Li, X. Wang, X. Liu, L. Shi, K. Wei, C. Ling, Z. Li and H. Wang, *Adv. Mater.*, 2021, **33**, 2100143.
48 Y. Shi, J. Li, C. Mao, S. Liu, X. Wang, X. Liu, S. Zhao, X. Liu, Y. Huang and L. Zhang, *Nat. Commun.*, 2021, **12**, 5923.
49 J. Zhao, Y. Mu, L. Wu, Z. Luo, L. Velasco, M. Sauvan, D. Moonshiram, J. Wang, M. Zhang and T. Lu, *Angew. Chem., Int. Ed.*, 2024, **136**, e202401344.
50 R. Fang, Z. Yang, J. Sun, C. Zhu, Y. Chen, Z. Wang and C. Xue, *J. Mater. Chem. A*, 2024, **12**, 3398–3410.
51 C. Ban, Y. Wang, J. Ma, Y. Feng, X. Wang, S. Qin, S. Jing, Y. Duan, M. Zhang, X. Tao, L. Gan and X. Zhou, *Chem. Eng. J.*, 2024, **488**, 150845.